RSC Advances

PAPER

View Article Online
View Journal | View Issue

Cite this: *RSC Adv.*, 2025, **15**, 18142

Tweaking the electrochemical potential of nitrogen-rich Ce-PTA-MOF with reduced graphene oxide for use as a hybrid supercapacitor†

Muhammad Shahbaz, [a] Shahzad Sharif, *[a] Tayyaba Tur Rehman Afzal,[a] Zaeema Iqbal,[a] Zainab Ghaznazvi,[a] Maham Saeed,[a] Ayesha Shahzad,[a] Abdulaziz Bentalib,[b] Abdulrahman Bin Jumah [b] and Sajjad Hussain [c]

The scarcity of efficient energy storage devices (ESDs) demands the design of hybrid supercapacitors that integrate the properties of batteries and supercapacitors into one unit. Amongst the various known electrode materials, metal–organic frameworks (MOFs), due to their high porosity and unique electrochemical features, have come forward to boost the electrochemical performance of ESDs. However, the low conductivity of MOFs hinders their practical applications, and researchers are trying to address this issue by designing various strategies that unlock their extraordinary potential. In this work, the conductivity of Ce-PTA-MOF derived from cerium and pyridine-2,4,6-tricarboxylic acid was tweaked by using different amounts of reduced graphene oxide (rGO). Analysis of the electrochemical performance in a three-electrode set up showed that the composite of Ce-PTA-MOF and rGO with a 1 : 2 ratio possessed a significant specific capacity of 689.56 C g^{-1} which indicated its suitability for use in practical applications. Hence, a hybrid supercapacitor was fabricated from Ce-PTA-MOF@rGO and activated carbon (AC) which exhibited a specific capacity of 380.83 C g^{-1}, a specific energy of 74 W h kg^{-1} and a specific power of 434 W kg^{-1} at 0.5 A g^{-1}. A coulombic efficiency of 99% was recorded even after 5000 GCD cycles. The remarkable stability and high specific energy and power density proved that this synthesized composite is a viable option for use in future energy storage devices.

Received 2nd March 2025
Accepted 8th May 2025

DOI: 10.1039/d5ra01490e

rsc.li/rsc-advances

1. Introduction

As non-renewable energy sources diminish with every passing day, renewable energy resources have become more attractive, which has triggered the need for energy storage devices (ESDs). Meanwhile, many portable electronic devices are gaining increasing interest because of sustainability challenges in the emerging world of smart networks.[1] Supercapacitors (SCs) have high specific powers (P_s)[2] and long life cycles,[3] whilst batteries have high specific energies (E_s).[4,5] A systematic strategy to unite both attributes in an individual device has attracted much attention from researchers. In this regard, the idea of developing hybrid supercapacitors (HCs) has been thoroughly investigated to overcome the constraints of traditional ESDs.[6,7] Even though numerous electrode materials have been reported for high-performance energy storage systems, but significant stability, high E_s and P_s have not been attained so far. To confront this challenge, MOFs have offered encouraging potential in light of their intrinsically possible specific structures, huge surface areas, large pore apertures, enhanced stability, novel electronic behavior, and efficient redox-activity.[8,9] MOFs are also used in ion-exchange, non-linear optics, gas storage, and separation in catalysis.[10] Supercapacitors (SCs) are promising energy storage devices but low energy densities have hindered their practical applications in energy storage. A new approach of constructing asymmetric supercapacitors with different positive and negative electrodes has attracked much attention of the researchers recently as it expands the voltage window and improves the energy density. Of the various electrode materials currently being investigated, metal–organic frameworks (MOFs) are being explored extensively due to their high porosity, tunable structures, and plentiful active sites.[11]

Numerous studies have demonstrated that MOFs provide exceptional capacities when utilized as an electrode material.[12] Furthermore, enhanced electrical conductance can be obtained by developing composites of MOFs with several functional substances to attain boosted redox properties.[13] Although different metals of the s, p, and d block have been studied for

[a]*Materials Chemistry Laboratory, Institute of Chemical Sciences, Government College University Lahore, 54000, Pakistan. E-mail: mssharif@gcu.edu.pk; Tel: +92 345 4579334*

[b]*Department of Chemical Engineering, College of Engineering, King Saud University, P.O. Box 800, Riyadh 11421, Saudi Arabia*

[c]*School of Pharmacy, Key Laboratory of Nano-carbon Modified Film Technology Engineering of Henan Province, Xinxiang University, Xinxiang 453000, PR China*

† Electronic supplementary information (ESI) available. See DOI: https://doi.org/10.1039/d5ra01490e

better oxidation–reduction reaction capabilities in ESDs, the desired improvements have not been achieved yet. Consequently, the research field has been widened to the lanthanide series which show incredible potential for applications in optoelectronic devices, captivating structures, monitoring systems, magnetization, ion substitution gas sorption, and materials chemistry.[14] Rare-earth ions that are engaged through polycarboxylate ligands show remarkable interaction strengths with electrophilic centers.[15] In addition, lanthanide-containing networks exhibit aqueous phase chemical durability and redox reversibility.[16]

Amongst the rare-earth metals, cerium possesses superb chemistry, relying strongly on its various oxidation states.[17] It is known for its oxidation attributes with different catalytic and optical properties in MOF chemistry.[18] Aromatic ligands with carboxylate functional groups are well known for their use in MOFs. Additionally, the incorporation of heteroatoms (N, S, and O) in the aromatic ring have improved the electrochemical performance.[19] Pyridine-2,4,6-tricarboxylic acid is an organic compound with a nitrogen atom present in the pyridine ring that also has three carboxyl groups which are involved in coordination with metal atoms. This structure enhances electrochemical performance, as compared to a simple benzene ring, due to the presence of the heteroatom (N) in the pyridine ring.[20,21] *Via* nitrogen incorporation, the MOFs electronic structure goes through considerable changes. The band gap is reduced by increasing the density of states close to the Fermi level when the nitrogen atom donates electrons. This boosts the mobility of charge carriers, allowing for proficient electron transfer. Zhang *et al.* described the development of hollow sheets of iron-doped cobalt sulfide with a double-shelled structure produced by placing a ligand in ZIF-L followed by sulfurization and then coating of CeO_2 through a solvothermal method. The Fe–CoS/CeO_2 electrode showed a high specific capacitance (3727.5 F g^{-1}) and energy density (36.4 W h kg^{-1}) with a cycling stability retention of 89.8% after 10 000 cycles.[22]

Additionally, incorporation of a conductive material can boost the conducting properties.[23] Usually, polythiopehene (PTh), polyaniline (PANI), polyacetylene (PA), poly(3,4-ethylenedioxythiophene) PEDOT and polypyrrole (PPy), which all have π-conjugated structures, facilitate the delocalization of electrons, leading to high conductivity by enabling dopants.[24,25] Furthermore, the electrochemical attributes of supercapacitor involving MOFs can also be increased by combining with carbon containing compounds including nanotubes (CNT), graphene oxide (GO) and reduced graphene oxide (rGO).[26] Better electrochemical properties of rGO pave the way for improved energy storage devices due to high carrier mobility and restored sp^2 hybridization. Ce-MOF is synthesized from 1,3,5-benzene tricarboxylic acid and its composites *i.e.* Ce-MOF/CNT and Ce-MOF/GO have been reported. The specific capacity of pristine Ce-MOF was recorded as 94.8 F g^{-1} and the composites of CNT and GO showed 129.6 and 233.8 F g^{-1}, respectively. Ce-BTC-MOF was also reported to form a CeO_2/rGO composite when exposed to a sulfidation process, yielding a CeO_2/rGO/CeS_2 nanocomposite. The increased conductive performance was confirmed by cyclic voltammetry (CV), chronopotentiometry (CP) and electrochemical impedance spectroscopy (EIS). In 3 M KOH electrolyte, the CeO_2/rGO/CeS_2 composite has a capacitance of 720 F g^{-1} with E_s and P_s values of 23.5 W h kg^{-1} and 2917.2 W kg^{-1}, respectively, at 2.5 A g^{-1}.[26] Hong *et al.* also reported the use of Ce-MOF/CNT composites as separators for coating materials in lithium sulphur batteries (LIB). When exposed to a high sulphur loading, the composite showed brilliant conducting attributes with better capacity retention results. A specific capacity of 1021.8 mA h g^{-1} was achieved which gradually decreased to 838.8 mA h g^{-1} after 800 cycles.[27] Ping Wen *et al.* also investigated a rGO/CMOF-5 composite, which achieved an impressive capacitance of 312 F g^{-1} at 0.5 A g^{-1} in basic electrolyte and an excellent capacitive retention of 89% even after 5000 GCD cycles.[28] A regular supercapacitor based on a rGO/CMOF-5 hybrid exhibited an E_s of 17.2 W h kg^{-1} at a Ps of 250 W kg^{-1}. MoO_3/rGO demonstrated a specific energy of 55 W h kg^{-1}, a specific density 400 of W kg^{-1} with a cycling stability of 87.5% after 6000 cycles.[29] Ni-doped MOFs with rGO demonstrated a specific capacitance of 758 F g^{-1}, compared with the original MOF which showed capacitance of 100 F g^{-1}, attributed to the integration of the rGO. A specific energy of 37.8 W h kg^{-1} and specific power of 227 W kg^{-1} was recorded.[30] A Ni/Co-MOF/rGO composite exhibits a specific capacitance of 958 F g^{-1} at 1 A g^{-1} with a capacitance retention of 109% even after 5000 GCD cycles. The study revealed enhanced electron transport and inhibition of MOF accumulation due to the rGO network.[31] These findings demonstrate that this hybrid approach leads to novel ideas for the consumption of old carbon substances whilst achieving excellent outcomes in energy storage devices.[28]

In continuation of our earlier reported work which focused on the incorporation of nitrogen-based linkers in Ce-PTA-MOF to enhance the electrochemical properties, this work has explored the effect of conductive material to unlock the extraordinary electrode potential of MOFs. A number of conductive materials, such as polyaniline (PANI) and polypyrole (PPY), along with graphene oxide (GO), carbon nanotubes (CNTs) *etc.* are being used today to improve the performance of synthesized materials. However, PANI, PPY and GO show limited electrical conductivity.[32] CNTs are a cylindrical/tubular shaped material with excellent mechanical stretching and high conductivity along the tube axis. In conversely, rGO has a flat, sheet-like 2D structure which provides excellent conductivity[33] and a large surface area for adsorption and reaction processes.[34] Owing to its large surface area, rGO was targeted to prepared MOF composites. The addition of rGO to Ce-PTA MOF improved the charge transfer kinetics. Composites of Ce-PTA-MOF were prepared by adding rGO in different ratios (1 : 1/CG 100, 1 : 2/CG-200, 1 : 3/CG-300) to optimize the electrochemical performance, as an excessive amount of rGO leads to aggregation which reduces the effective surface area and ion diffusion.[35] Ce-PTA-MOF provides redox active sites and rGO improves the conductivity and the synergistic effect.[36,37] Electroanalytical techniques including CV, GCD and EIS were applied to understand the electrochemical performance. In a three-electrode set up with 6 M KOH electrolyte, CG-200 was confirmed to improve the electrochemical performance

showing a specific capacity of 689.56 C g^{-1}. This compelled us to demonstrate its practical application in a hybrid supercapacitor assembly against activated carbon (AC). The device showed Es and Ps values of 74 W h kg^{-1} and 434 W kg^{-1}, respectively, with a coulombic efficiency of 99% even after 5000 GCD cycles. The extraordinary electrochemical performance underscores the high potential of the prepared composite for futuristic hybrid supercapacitors.

2. Synthesis and experimental

2.1. Chemicals

All the chemicals, such as reduced-graphene oxide, *N*-methyl-2-pyrrolidone, polyvinylidene fluoride, potassium hydroxide, ethanol and activated carbon were procured from Sigma-Aldrich and further used without purification.

2.2. Synthesis of cerium-metal organic frameworks (Ce-PTA-MOF)

Ce-PTA-MOF was synthesized by adopting our reported method.[38]

2.3. Synthesis of Ce-PTA-MOF@rGO electrodes

4.5 mg of Ce-PTA MOF were mixed with different ratios of rGO (1 : 1, 1 : 2 and 1 : 3) in three separate vials. 0.5 mg of a polyvinylidene fluoride (PVDF) binder was added to the composite mixture and *N*-methyl-2-pyrrolidone (NMP) solvent was poured over the mixture. The mixture was stirred for 6 h at room temperature to make a homogeneous slurry. Meanwhile, a nickel foam (NF) was conditioned by subsequent rinsing with 1 M HNO_3, water and ethanol. Three electrodes, Ce-PTA@rGO-100 (CG-100), Ce-PTA@rGO-200 (CG-200) and Ce-PTA@rGO-300 (CG-300), were prepared by adopting drop casting techniques. The as-prepared electrodes were dried at 70 °C for 6 h for electrochemical characterization (Fig. 1). For CG-100 (1 : 1), 6.0 ± 0.2 mg was deposited on the electrode whereas 9.0 ± 0.2 mg and 12.0 ± 0.2 mg were deposited for CG-200 (1 : 2) and CG-300 (1 : 3), respectively.

The ASC device was assembled using Ce-PTA@rGO as the positive electrode and activated carbon (AC) as the negative electrode with 6 M KOH aqueous solution as the electrolyte. For the two electrode assembly, a slurry of AC was prepared according to eqn (1) (ref. 39) and drop casted by following the same procedure mentioned above. The mass of carbon was estimated to be double the mass of the active material of the positive electrode.

$$\frac{m_+}{m_-} = \frac{C_{s-} \times \Delta V_-}{Q_s} \quad (1)$$

Q_s represents the specific capacity of the anode, m denotes the active mass of both electrodes and ΔV corresponds to the operating voltage window. The ratio of masses between the positive and negative electrodes was 1 : 2.

The value of b differentiates between diffusion-controlled current and a surface-controlled capacitive process and can be calculated from the slope of a plot between log of peak current (i) and log of scan rate (v). Eqn (2) and (3) represent the relation between the b value and peak current:[40]

$$i = av^b \quad (2)$$

$$\log(i) = \log(a) + b\log(v) \quad (3)$$

'a' and 'b' are adjustable constants, 'i' denotes the peak current whereas 'v' corresponds to the scan rate. Dunn's equation (eqn (4)) can be utilized to investigate the kinetic mechanisms to differentiate between capacitive and diffusive processes.[41]

$$i(V) = k_1 v + k_2 v^{1/2} \quad (4)$$

Here, k_1v denotes the fast surface capacitive effect, $k_2v^{1/2}$ represents the diffusion controlled reaction, 'i' is the peak current and V corresponds to the scan rate. From the CV profile, the specific capacity (Q_s) and specific capacitance (C_s) were calculated using eqn (5) and (6). For a non-symmetric GCD curve due to a quasi-reversible faradaic reaction, the ratio of the faradaic reaction charge/voltage does not remain constant and changes with time. Hence, eqn (7)–(10) were used to determined C_s, Q_s, E_s and P_s.[42]

$$Q_s = 2\frac{I}{m}\frac{\int_{v^i}^{v^f} dV}{V} \quad (5)$$

$$C_s = 2\frac{I}{m}\frac{\int_{v^i}^{v^f} dV}{V^2} \quad (6)$$

$$Q_s = 2\frac{I}{m}\frac{\int_{v^i}^{v^f} dV}{V^2} \quad (7)$$

$$C_s = 2\frac{I}{m}\frac{\int_{v^i}^{v^f} dV}{V^2} \quad (8)$$

$$E_s = \frac{I}{m}\frac{\int_{v^i}^{v^f} dV}{3.6} \quad (9)$$

$$P_s = E_s \times \frac{3600}{td} \quad (10)$$

2.4. Crystallographic data collection and refinement

The diffraction experiments were performed at 296 K and the procedures involved in the analysis were: data collection: COLLECT,[43] cell refinement: DENZO/SCALEPACK,[44] and data reduction: DENZO/SCALEPACK. The program(s) used for the molecular graphics were as follows: the Mercury program.[45] The software used to prepare material for publication: WinGX.[46] All non-hydrogen atoms were refined with anisotropic parameters.

3. Result and discussion

3.1. Structural characterization

3.1.1. Description of structures. The asymmetric unit of the Cu-PTA-MOF consists of two Ce(III) ions, three coordinated water molecules, two non-coordinated water molecules, one

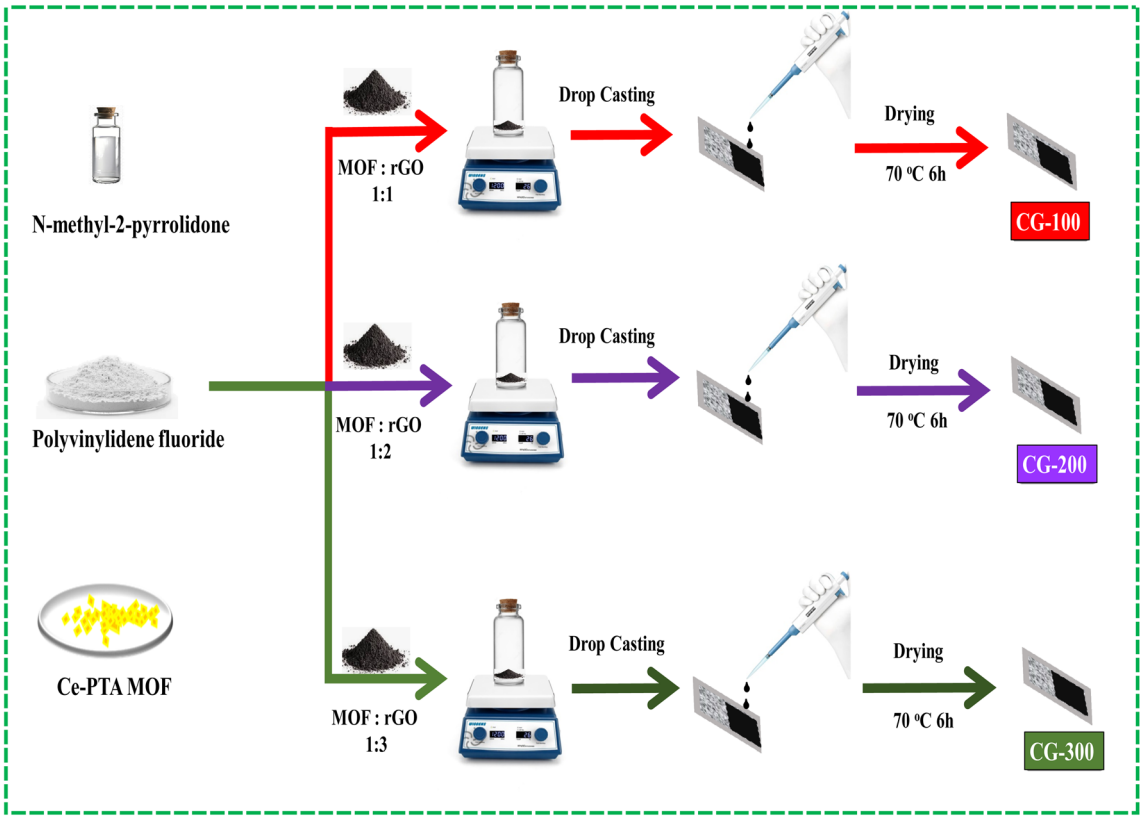

Fig. 1 Synthesis of the Ce-PTA-MOF@rGO electrodes.

ammonia molecule and two pyridine-2,4,6-tricarboxylic (PTA) ligands (Fig. 2A). A schematic polyhedral view of the 3D propagation along the 001 direction of the Ce-3D polymer is shown in Fig. 2B and C, while a polyhedral view showing a spherical pore of dimensions 2.7 × 2.3 nm is shown in Fig. 2D. Details of the crystal structures are given in Table S1.† The coordination bond lengths are reported in Table S2† and the hydrogen-bond parameters are provided in Table S3.†

3.1.2. Thermogravimetric analysis (TGA) and Fourier-transform infrared (FTIR) spectroscopy. The confirmation of the structure was also carried out using TGA and FTIR spectroscopy, details of which are provided in the ESI (Fig. S1 and S2).†

3.2. Electrochemical characterization

Electrochemical testing was performed utilizing the electrochemical workstations OrigaFlex-OGF01A and OrigaFlex-OGFEIS. The as-prepared electrodes of Ce-PTA-MOF, CG-100, CG-200 and CG-300 were used as the working electrodes (cathode) in a three electrode assembly with platinum wire as a counter electrode and Hg/HgO as the reference electrode in an electrolyte of 6 M KOH.

3.2.1. Half-cell electrochemical analysis

3.2.1.1 Cyclic voltammetry (CV). In electroanalytical chemistry, CV is a very important technique which is simple and inexpensive. It provides information about the thermodynamics and kinetics of redox processes.[47] It is very helpful in the quantitative study of various complex chemical setups like the modification of electrodes with specific deposits.[48] The inherent electrochemical properties of CG-100, CG-200, and CG-300 were investigated using cyclic voltammetry (CV) at various scan rates (5, 10, 20, 30, 40, and 50 mV s^{-1}) within a potential window of 0 V to 0.5 V (Fig. 3a to c). The CV peaks of all the curves shifted towards a higher potential during the forward scan and to a lower potential scan during the backward scan. The shapes of the CV curves also become broader. The voltammograms obtained at a fast scan rate turned out to be complicated due to solution resistance attributed to ohmic drop (IR), sluggish charge transfer reaction rates, capacitive currents and instrument delay. At lower scan rates, the potential shift is not significant but it becomes more and more prominent at higher scan rates.[49] At higher scan rates, the electroactive species do not have enough time to intercalate in the pores of the material which creates a concentration gradient around the electrode, resulting in peak potential shift. Furthermore, a higher capacitive current also distorts the voltammogram, and the electron transfer kinetics do not keep up with the applied potential; therefore, a shift in the peak potential is generally observed. At a scan rate of 5 mV s^{-1} (Fig. 3a to c), a significant increase in current was observed after 0.3 V, which reached a maximum around 0.4 V and then deceased steadily before reaching 0.45 V. A sharp increase in the current after 0.45 V was also detected and was attributed to side reactions, commonly attributed to oxygen-evolution. It was observed that an increase in the scan

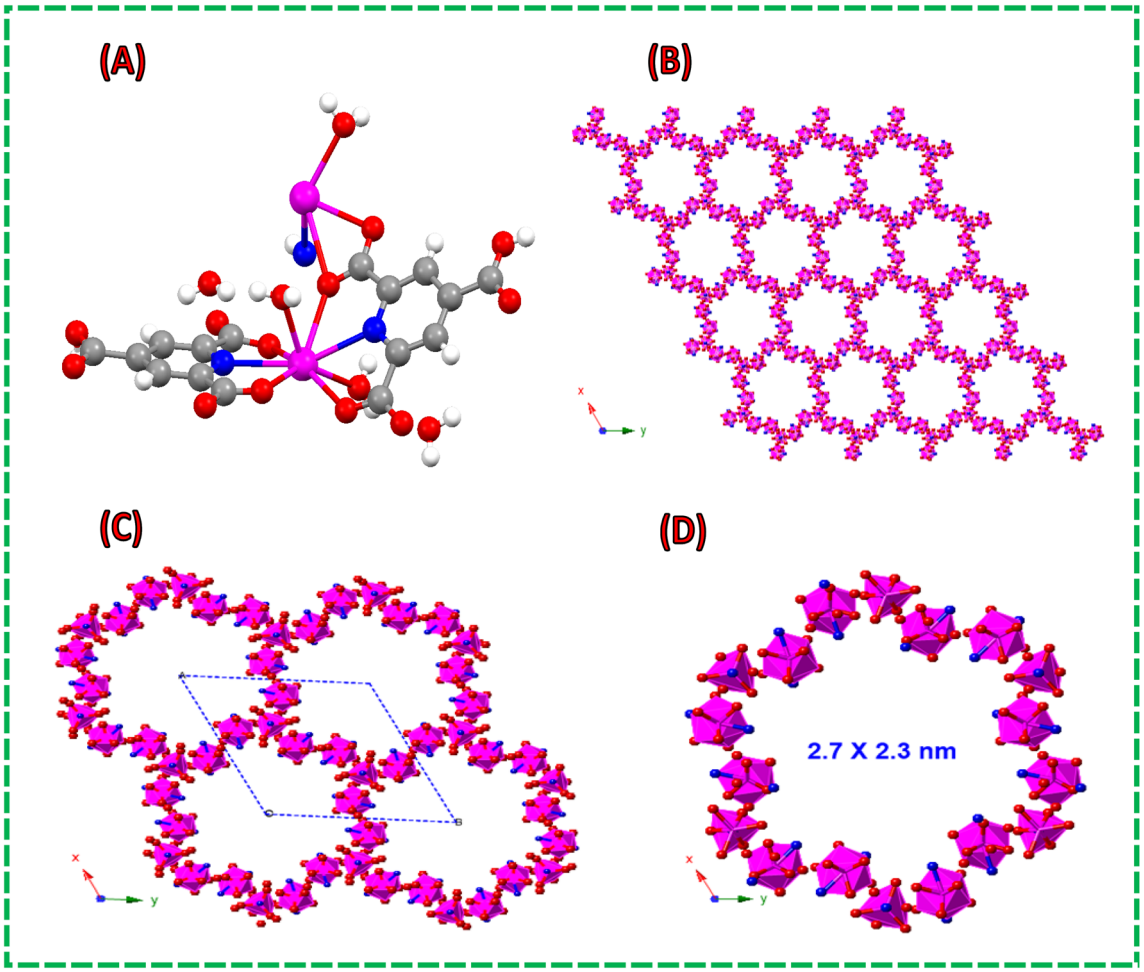

Fig. 2 (A) The asymmetric unit of the Ce-3D polymer, colour of atoms: magenta: cerium, blue: nitrogen, red: oxygen, black: carbon, white: hydrogen. (B and C) Schematic polyhedral view of 3D propagation along the 001 direction in the Ce-3D polymer. (D) Polyhedral view showing a spherical pore.

rate shifted the peak current towards higher potential due to IR-drop, sluggish charge transfer reaction rates, capacitive currents and instrument delay. At a higher scan rate of 50 mV s^{-1}, the peak current was shifted around 0.45 V and decreased to 0.5 V. If a higher scan rate was applied, the potential window would have moved further toward higher potential. It is very tricky to select a suitable potential window for cyclic voltammetry. A potential window from 0 V to 0.5 V was selected only to show the complete CV curve at higher scan rates. However, for the purpose of GCD analysis, a 0.4 V potential was selected to avoid problems associated with higher scan rates and current density. It is suggested that the CV curve at lower scan rates should be studied to select the potential used in the GCD analysis. The shape retention of a CV peak refers to the consistency over multiple cycles or repeated measurements. As the scan rate increased, the peaks became broader, thus showing the increase in the capacitive contribution. A comparison of the CV curves for all the samples at 10 mV s^{-1} scan rate confirmed that CG-200 had the highest charge storage area (Fig. 3d). A plot of the square root of the scan rate against the peak current has a regression coefficient of 0.9, illustrating the reversibility of the oxidation/reduction reaction (Fig. 3e). Comparison of the specific capacities of CG-100, CG-200 and CG-300 illustrated that CG-200 exhibited the maximum value of 687.8 C g^{-1} (Fig. 3f).

In addition, the *b* value was determined to differentiate between diffusion-controlled current and a surface-controlled capacitive process. The *b* value helps to understand the nature of the material such that a *b* value near 1 signifies a capacitor-like material, a value nearing 0.5 denotes a battery-like nature, whilst a *b* value around 0.8 corresponds to a pseudocapacitive nature. The power-law relationships were used to get the *b* values for CG-100, CG-300 and CG-200 (Fig. S3a, b† and **4a**). CG-100 showed a *b* value of 0.74 (oxidation) and 0.76 (reduction) and for CG-300 it was recorded as 0.59 (oxidation) and 0.63 (reduction). CG-200 demonstrated a *b* value of 0.58 for the oxidation peak current and 0.60 for the reduction peak current which signified the predominance of battery-like behavior. The predominance of pseudocapacitive behavior is due to reversible faradaic redox reactions mainly because of the Ce^{4+}/Ce^{3+} couple and the pyridine and carboxylic functional groups of PTA at the interface of the electrode–electrolyte.[50,51] Additionally, the

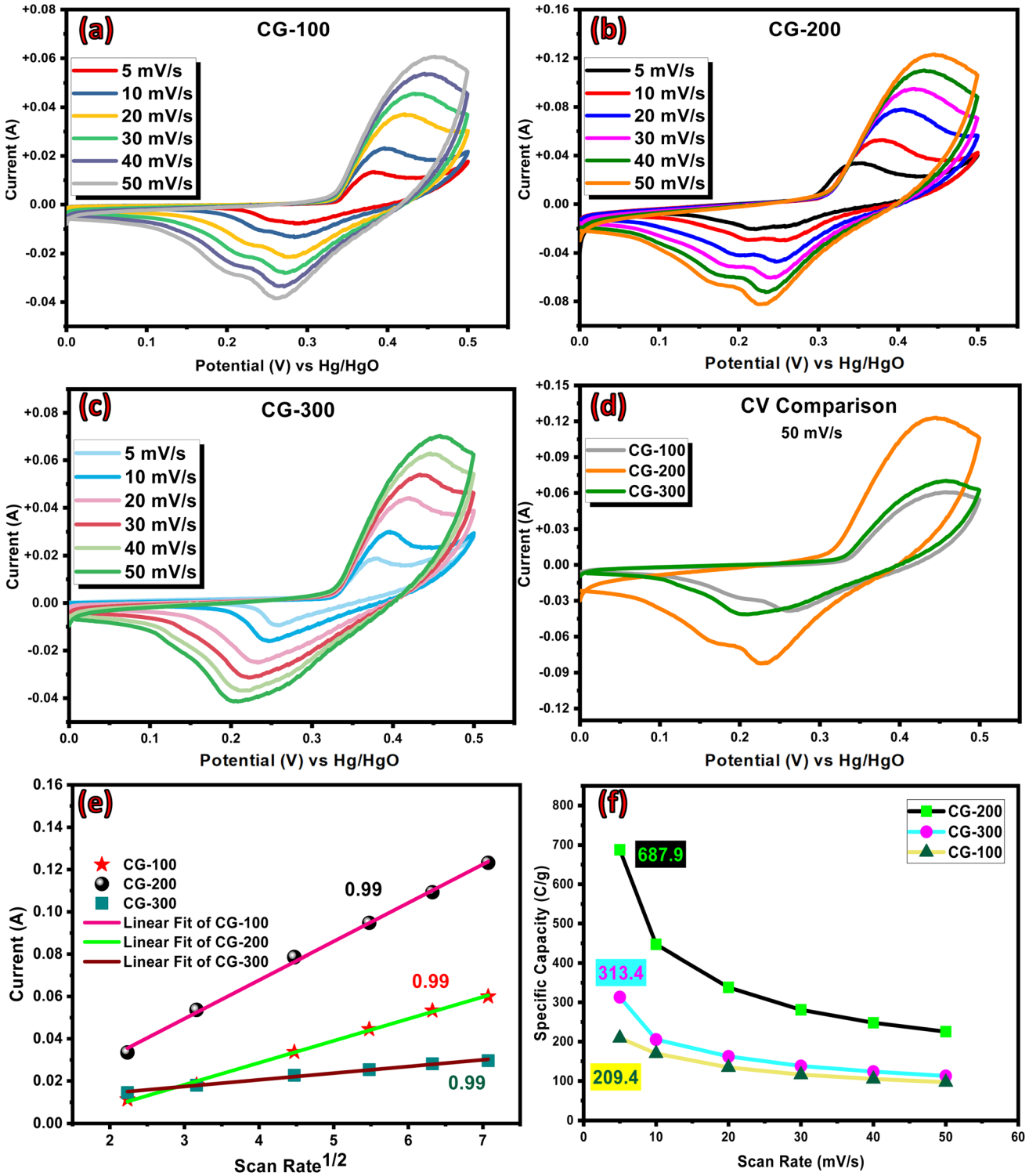

Fig. 3 (a) CV curves of CG-100 (b) CG-200 and (c) CG-300 at different scan rates. (d) Comparison of CV curves at 50 mV s^{-1} scan rate. (e) Values of the regression coefficients for CG-100, CG-200 and CG-300. (f) Relative specific capacity plots for CG-100, CG-200 and CG-300.

oxygen-containing functional groups in the rGO contribute to improving the conductivity and the redox reactions.[52] The Ce-PTA@rGO composite stores charge through redox reactions and electric double-layer capacitance (EDLC). The redox reaction of Ce^{4+}/Ce^{3+} in the MOF[53] provides the faradaic contributions, as shown in eqn (11), and all the non-faradic reactions are associated with the rGO component, as per eqn (12).

$$Ce^{4+} + e^{-} \leftrightarrow Ce^{3+} \quad (11)$$

$$q = C_{EDLC} \times V \quad (12)$$

The diffusive and surface-controlled contributions can be estimated through Dunn's method.[54,55] The high conductivity of rGO ensures fast electron and ionic transport whereas the porous structure and high surface area of the Ce-PTA MOF facilitates ion adsorption. Cerium metal centers contribute additional charge storage leading to a higher specific energy density. The composites of Ce-PTA with rGO have enhanced electrochemical properties due to a synergistic effect.[52]

In Fig. S4a,† the % capacitive/diffusive contributions of CG-100 are displayed in a bar graph. The diffusive contributions are mostly higher than the capacitive contributions in CG-300 (Fig. S4d†). The column plot for CG-200 (Fig. 4b) clearly displays the diffusive contributions. The contributions of the Faradaic/non-Faradaic and the overall current in the CV curves of CG-100, CG-300 and CG-200 at 10 mV s^{-1} are presented in Fig. S4b–c† and at 50 mV s^{-1} in Fig. S4c, d and f.†

3.2.1.2 Galvanostatic charge–discharge (GCD). To determine the energy storage capability, power capacity, efficiency of a device, and the cycle life, the electrode material behavior needs to be examined by applying a constant current as a function of time while recording the voltage during charging and discharging conditions. CG-100, CG-200 and CG-300 were subjected to charging-discharging at discrete current densities ranging from 1 to 7 A g^{-1} (Fig. 5a to c). For all the composites, an increase voltage during charging gave a non-linear region or plateaus, which was also observed on current reversal. This in agreement with the CV measurements, and CG-200 showed predominantly battery-like properties as evaluated by the shape of the graph and the discharge time at various current densities. The specific capacities of CG-100, CG-200 and CG-300 were 368.6, 689.56 and 229.46 C g^{-1}, respectively. These results showed that CG-200 has the best energy storage outcomes.

3.2.1.3 Electrochemical impedance spectroscopy (EIS). To uncover the conductivity of the electrode materials, a superior electrochemical technique, EIS, was used to differentiate the physical, electrical and electrochemical processes. These time-dependent processes are significant parameters for the evaluation of the variable resistance processes of boundary conductivities, charging/discharging, kinetics of charge transfer reactions and capacitive/diffusive nature of a material. The

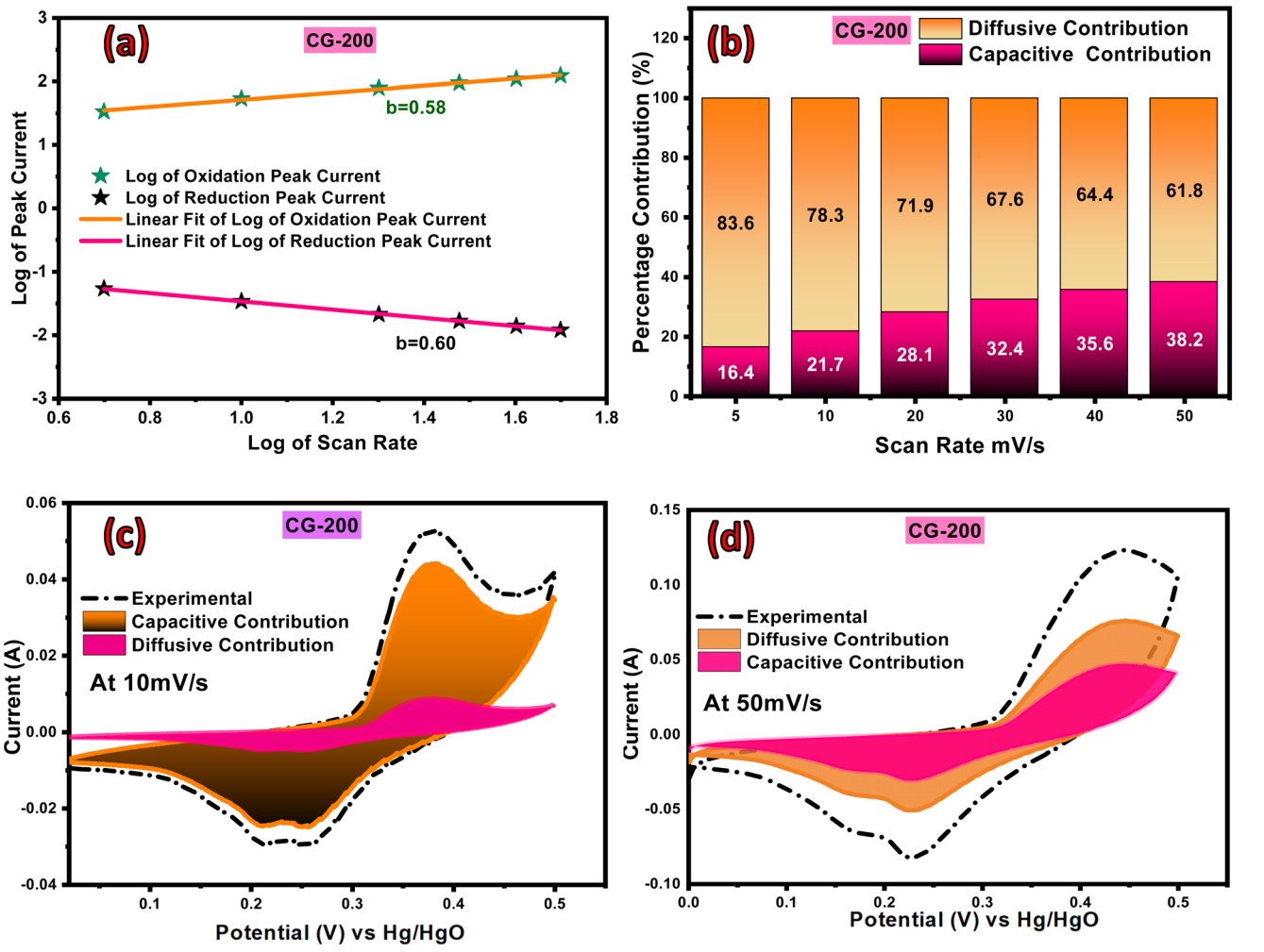

Fig. 4 (a) Plot of *b* values for CG-200. (b) Capacitive/diffusive contribution chart for CG-200. (c) Comparison of diffusive, capacitive and experimental CV curves of CG-200 at 10 mV s^{-1} and (d) at 50 mV s^{-1}.

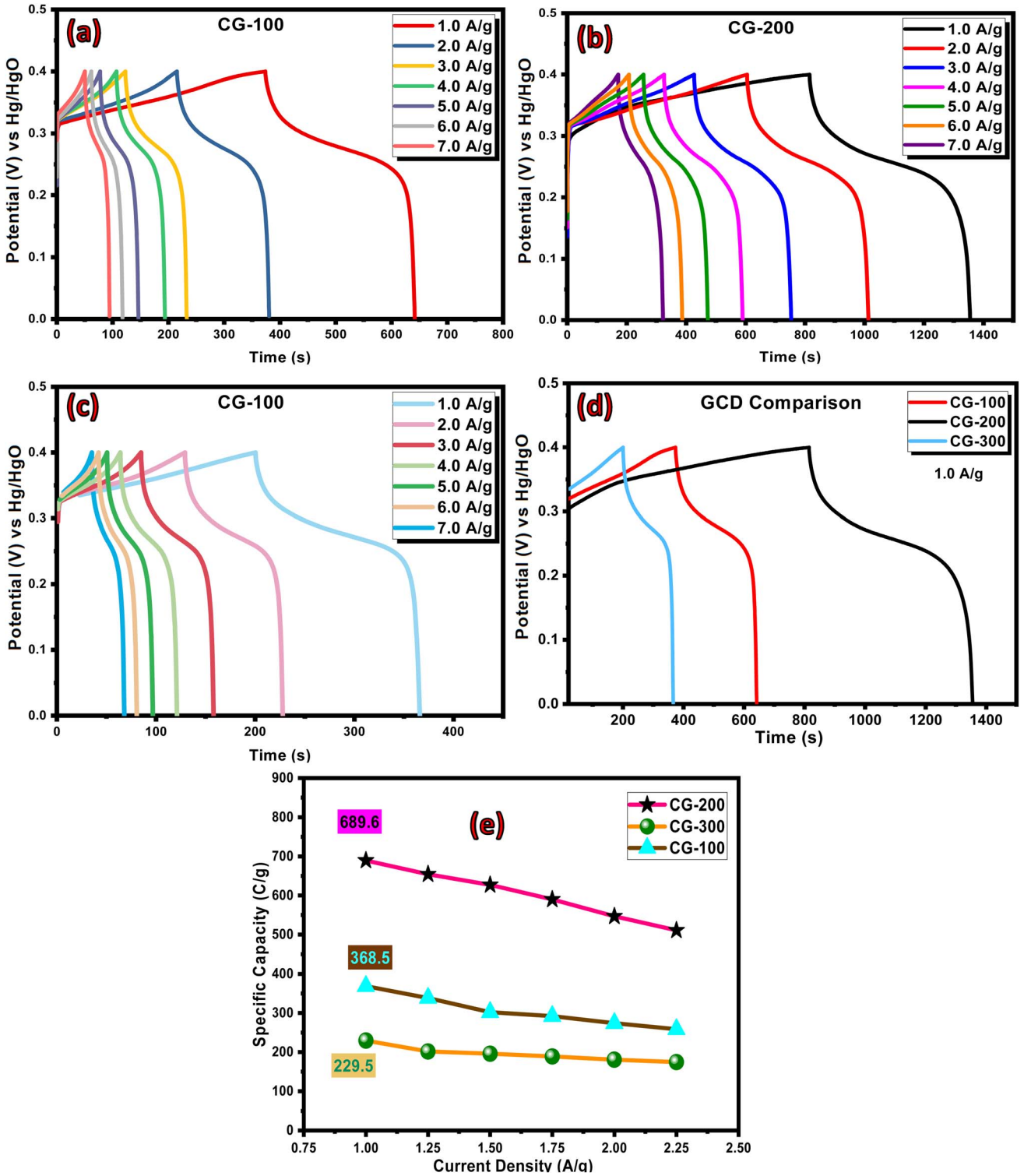

Fig. 5 Galvanostatic plateaus of (a) CG-100, (b) CG-200, and (c) CG-300 at various current densities. (d) Comparison of the GCV profiles of the composites at 1 A g^{-1}. (e) Comparison of the specific capacities.

Nyquist plot between the real part of the impedance (Z_r) and imaginary part of the impedance (Z_i) in an alternative current frequency range from 0.1 Hz to 100 kHz yielded an EIS plot with the equivalent circuit fitting for CG-100, CG-200 and CG-300 (Fig. 6a). The high frequency region corresponds the real part of the impedance (Z) and where the curve intercepts the abscissa (real axis) in the Nyquist plot indicates the equivalent series resistance (ESR). The ESR is crucial value for batteries and capacitors as it reflects energy losses due to two types of resistance, *i.e.*, solution resistance and any resistance between the

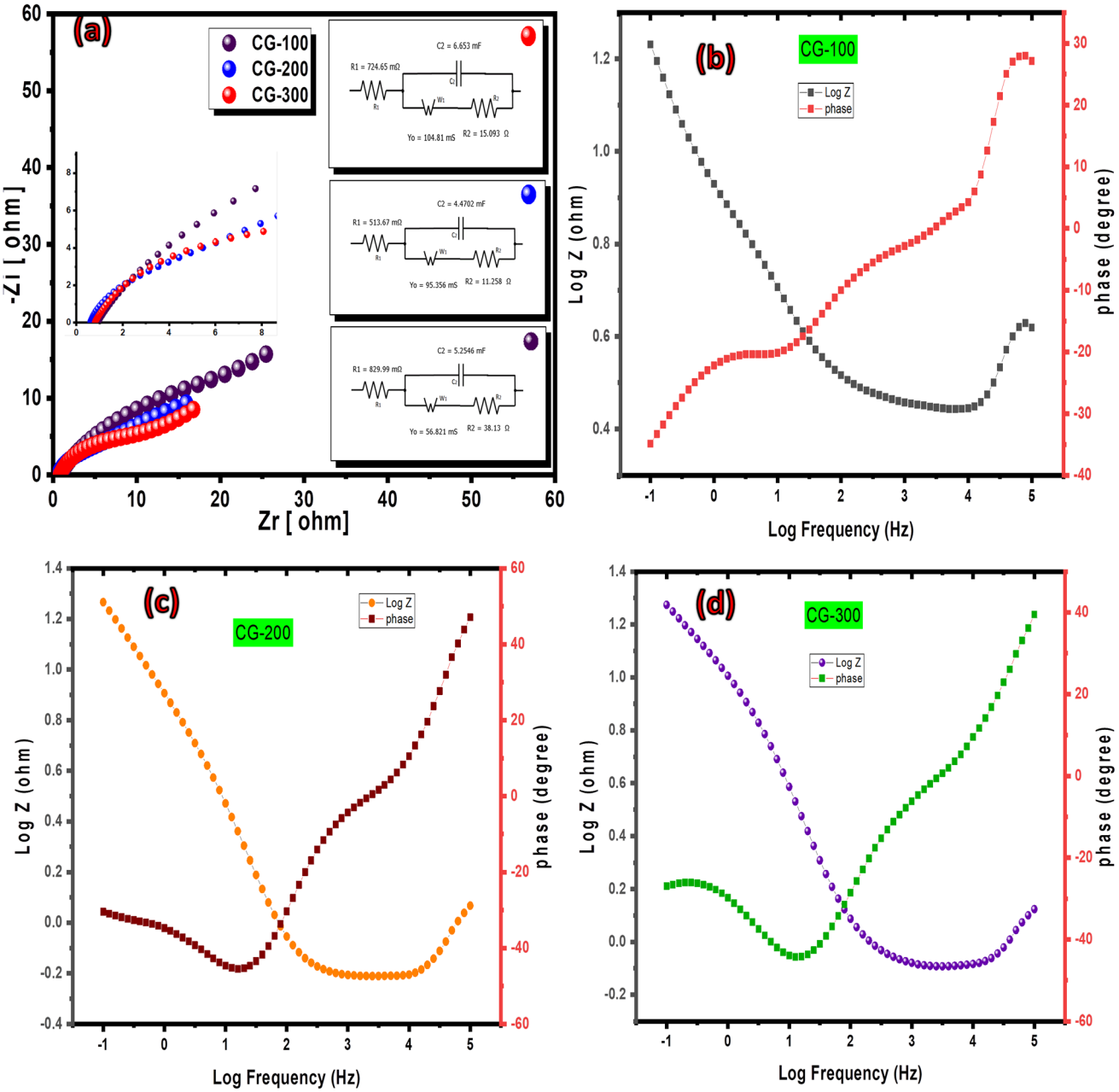

Fig. 6 (a) EIS results for CG-100, CG-200 and CG-300. (b) Bode phase angle plot for the electrodes of CG-100 (c) CG-200 and (d) CG-300.

electrode and the current collector interfaces or other elements. The R_{ct} is found in the mid or high frequency region and the form of the semi-circle which corresponds to the imaginary part of the impedance reflects the resistance to charge transfer at the electrode/electrolyte interface in an electrochemical reaction. Here, the higher the R_{ct} the slower the charge transfer process. Moreover, the line at a 45° angle in the high frequency region shows the Warburg resistance (Z_w) due to mass transport restrictions, specifically for ion diffusion in the electrolyte. The ESR value in the case of CG-100 was 0.8 Ω, for CG-200 it was 0.5 Ω and for CG-300 it was 0.7 Ω, showing that CG-100 has the highest ohmic and contact resistance and that CG-200 has the lowest. Similarly the bigger semi-circle diameter of CG-100 shows that it has the highest R_{ct} value of 38.13 Ω, while the semi-circle of CG-300 showed a R_{ct} of 15 Ω and CG-200 exhibited the lowest R_{ct} value of 11.2 Ω having the smallest semi-circle. Also, CG-100 displayed higher Warburg resistance with the highest extended line at an almost 60° angle, indicating that CG-200 showed the most positive outcomes in the analysis. Bode phase angle plots for the electrodes of CG-100, CG-200 and CG-300 are shown in Fig. 6b to d.

rGO showed a strong synergistic interaction with Ce-PTA-MOF through π–π interactions which improved the electrical conductivity by forming a continuous conductive network, which not only prevented agglomeration of the MOF but also helped to maintain the accessible surface area.[56,57] The composite of Ce-PTA-MOF and rGO with a 1 : 2 ratio showed the best performance as the structural integrity was maintained, the

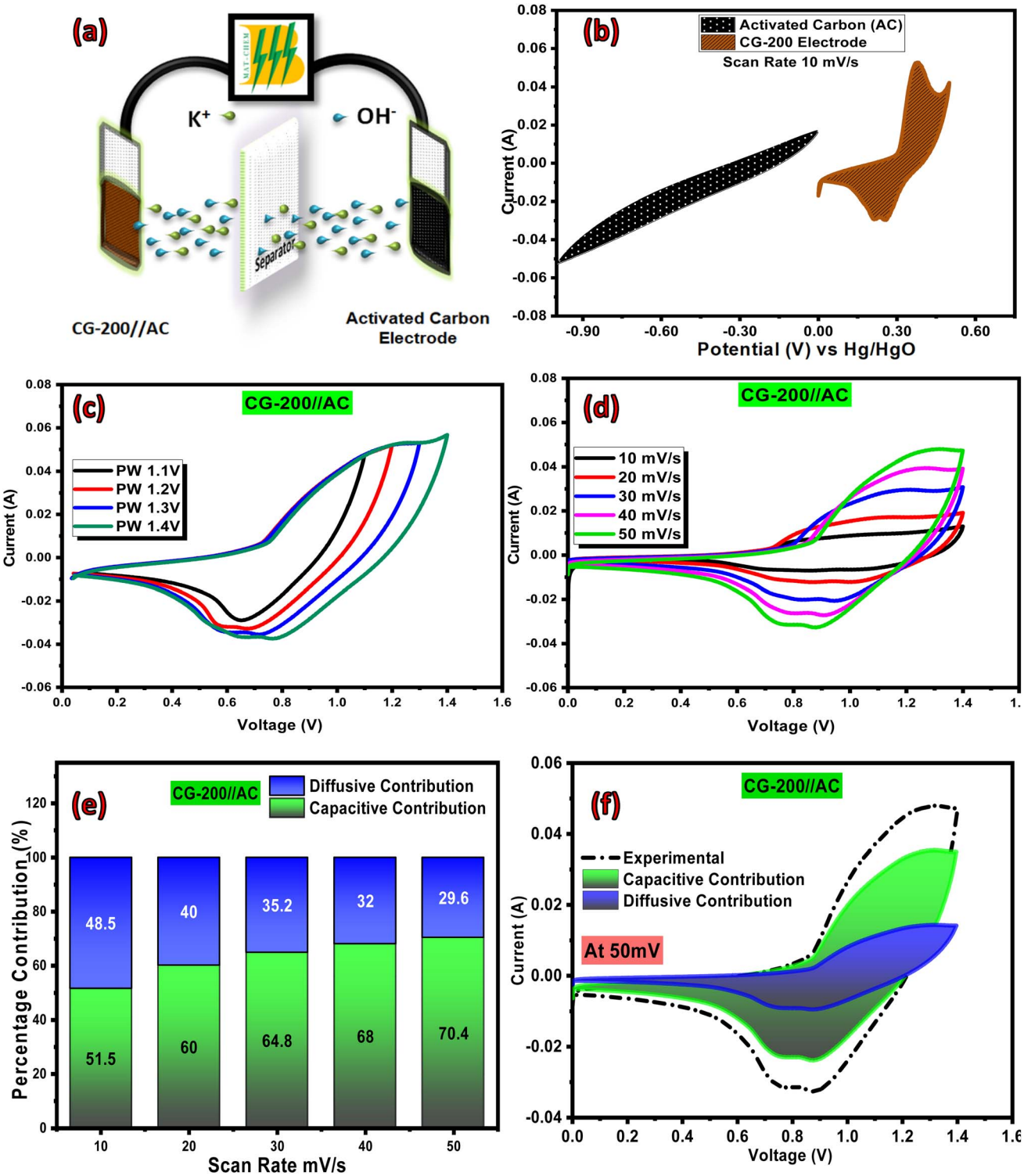

Fig. 7 (a) Design of the CG-200//AC hybrid assembly. (b) CV of CG-200 and AC in a three-electrode set up. (c) CV profiles of CG-200//AC in various potential windows. (d) CV curves of CG-200//AC. (e) Diffusive and capacitive percentage contributions of CG-200//AC at various scan rates. (f) Diffusive, capacitive and experimental CV curves at 50 mV s^{-1}.

conductivity enhanced by efficient ion transport, and the stability was improved, thus helping to achieving a high energy storage capacity.[1]

3.2.2. Hybrid supercapacitor assembly. The remarkable properties of CG-200 compelled us to develop a real device CG-200//AC comprised of activated carbon (AC) as the negative electrode and Ce-PTA@rGO (CG-200) as the positive electrode, separated by filter paper dipped in 1 M KOH electrolyte (Fig. 7a). The CV profile of the AC electrode exhibits a rectangular capacitive shape, while the CV profile of the Ce-PTA@rGO

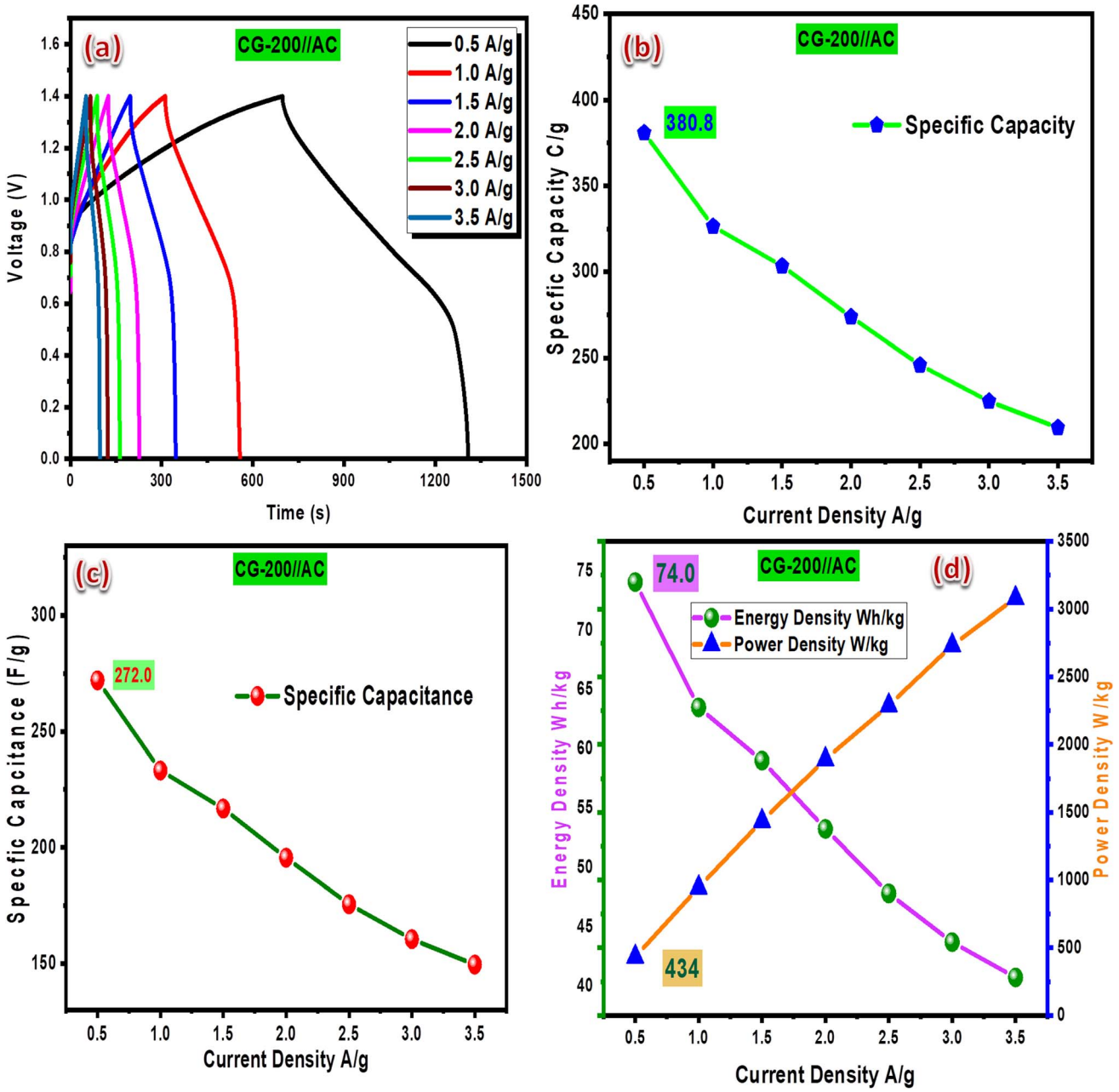

Fig. 8 (a) GCD of CG-200//AC at various current densities. (b) Specific capacity and (c) specific capacitance of the device with escalating current density. (d) Plot depicting the specific energy and specific power of the hybrid device.

composite shows battery-type characteristics with broad redox peaks (Fig. 7b). The potential window for the hybrid device was estimated from the CV curves of the AC and CG-200 electrodes in a three-electrode set up which was also confirmed by running the hybrid device at different voltages (Fig. 7c). The shape of the CV curves at different potential sweep rates ranging from 10 to 50 mV s^{-1} confirmed the pseudocapacitive nature of the device (Fig. 7d). The value of the regression parameter was recorded as 0.99 which verified the reversibility of the device (Fig. S6A†). The *b* value of 0.87 for the oxidation peak and 0.88 for the reduction peak (Fig. S6B†) also established the predominance of capacitive behavior in the hybrid device. Dunn's method was also used to adjudge the nature of device and a pronounced capacitive part was found. Fig. 7e illustrates how well the device performed as it shows a continuous increase in the capacitive contribution with increasing scan rate. The diffusive contribution (in blue) and capacitive contribution (in green) at 50 mV s^{-1} are with the experimental value (dashed black line) in Fig. 7f. Ineffective redox reactions or a high incidence of the EDLC at high scan rates are the main causes of the increase in the capacitive contribution. These results confirm that the assembled device exhibits a dominantly pseudocapacitive nature, arising from the synergistic effects of both surface capacitive and diffusion-controlled processes.[11,58]

The practical applicability of the hybrid device was assessed through GCD at various current densities ranging from 0.5 to 3.5 A g^{-1}, as shown in Fig. 8a. The asymmetry in the galvanostatic curves suggested the concurrence of both faradaic and non-faradaic reactions, denoting the combination of both diffusive and capacitive components. The impressive specific capacity and specific capacitance of the device was quantified using the formulas for non-symmetrical curves yielding 380.83 C g^{-1} and 272 F g^{-1}, respectively, at a current density of 0.5 A g^{-1}, as shown in Fig. 8b and c. The increased current

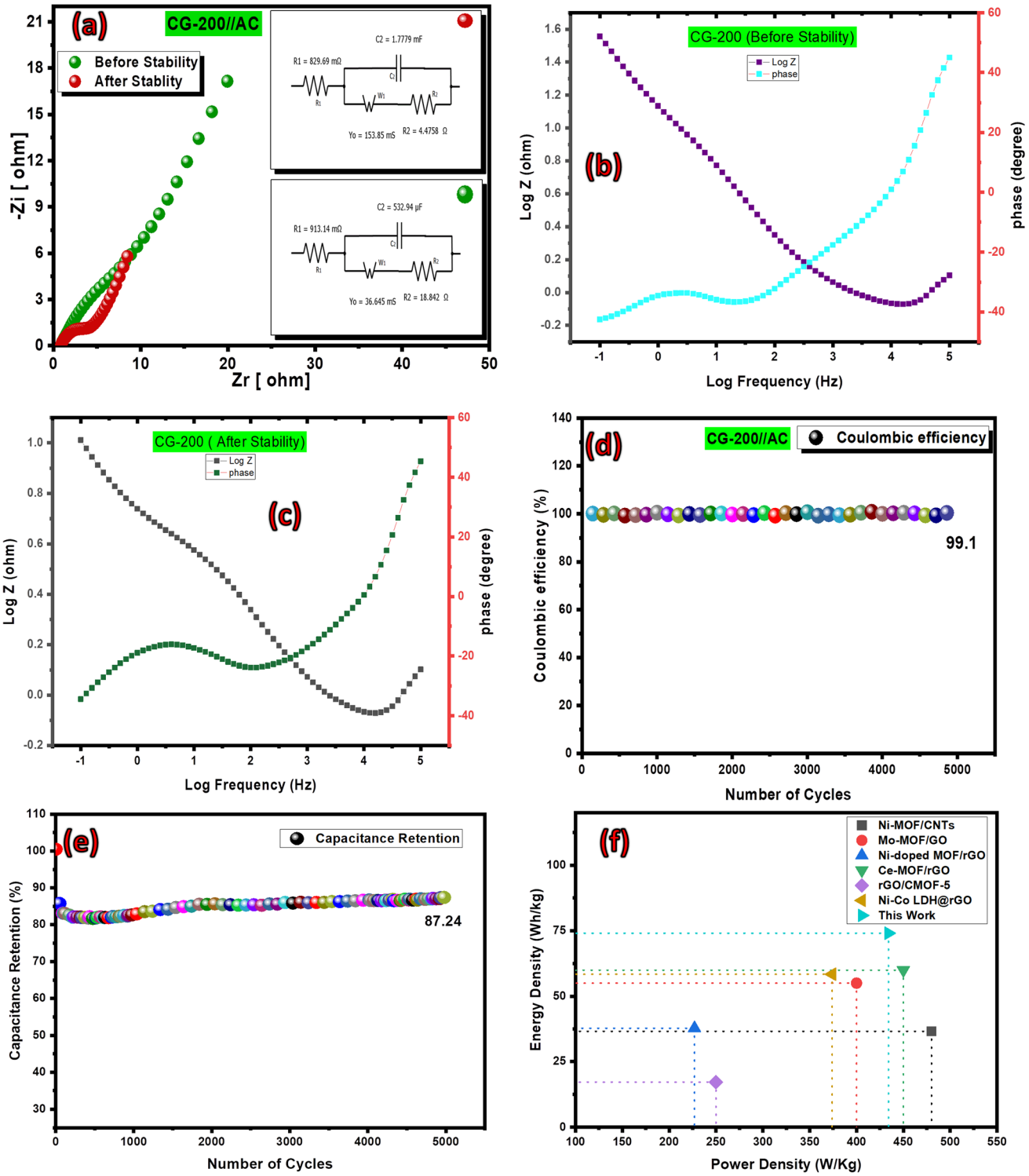

Fig. 9 (a) EIS illustration of hybrid device before and after stability test. Bode phase angle plot for the CG-200 device (b) before stability test and (c) after stability test. (d) Cyclic stability plot of the CG-200//AC device for 5000 GCD cycles. (e) Capacity retention of the device after 5000 cycles. (f) Ragone plot showing a comparison of the present work with previously reported MOFs materials.

Table 1 A comparison of current study with recently reported MOFs

Material	Electrolyte	Current density A g^{-1}	Specific energy (W h kg^{-1})	Specific power (W kg^{-1})	Ref.
CeO_2/rGO/CeS_2	3 M KOH	2.5	23.5	2917	26
rGO/CMOF-5	6 M KOH	2.0	17.2	250	28
rGO/MnO_3	H_2SO_4	2.0	55	400	29
Ni-doped MOF/rGO	1 M KOH	—	37.8	227	30
Ni-MOF/rGO-300	6 M KOH	1.0	17	750	31
Ce-MOF/rGO	3 M KOH	—	60	450	59
Ce-PTA	6 M KOH	1.0	26.75	5760	Previous work
Ce-PTA@rGO	6 M KOH	0.5	74	434	This work

densities decreased the capacities due to the potentially inadequate interaction time of the ions with the electrode. Using eqn (9) and (10), the specific energy (E_s) and specific power (P_s) were calculated and plotted against the current density (Fig. 8d). The device showed an impressive specific energy of 74 W h kg^{-1} at 0.5 A g^{-1} and a specific power of 3080.62 W kg^{-1} at 3.5 A g^{-1}.

The performance of the hybrid supercapacitor is closely associated with its conductivity, which can be gauged using EIS. Before and after running 5000 GCD cycles, EIS plots and their corresponding Randle's circuits were obtained (Fig. 9a). This revealed better results after the stability test. A small semi-circle (R_{ct} of 4.47 Ω), reduced Z_w line, and lower ESR (0.83 Ω) were recorded after running the stability test. The Bode phase angle plot for the device before and after the stability test is shown in Fig. 9b and c. Furthermore, the CG-200//AC device showed a coulombic efficiency of 99% even after 5000 GCD cycles (Fig. 9d). The capacity retention was 87.24% after 5000 charge–discharge cycles (Fig. 9e). A comparison of the present work with previously reported MOFs materials is also given in the Ragone plot in Fig. 9f.

4. Conclusions

Ce-PTA-MOF was synthesized from pyridine-2,4,6-tricarboxylic and was structurally characterized. No doubt, the use of heteroatomic linkers in the MOFs enhances its electrochemical properties yet the full potential of this unique class of MOFs has not been successfully unlocked. In continuation of our previous work,[38] the process of tweaking the electrochemical performance of Ce-PTA-MOF with highly conductive rGO has been targeted in the present research. Different percentages of rGO were amalgamated with Ce-PTA-MOF (CG-100, GC-200 and CG-300), and their electrochemical properties were analyzed in a three-electrode assembly using various electroanalytical tools including CV, GCD and EIS. CG-200 showed the best performance with a specific capacity of 689.56 C g^{-1} at 0.5 A g^{-1}. Hence, a device consisting of CG-200 and AC was fabricated to construct a hybrid supercapacitor (CG-200//AC). Dunn's methodology was employed to validate the pseudocapacitive nature of the device. The device showed a specific capacity, specific energy and specific power of 380.83 C g^{-1}, 74 W h kg^{-1} and 434 W kg^{-1}, respectively, at 0.5 A g^{-1} with a coulombic efficiency of 99%, even after 5000 GCD cycles, thus underscoring the composite as potential candidate for use as an energy storage device. Table 1 shows a comparison of the current study with recently reported materials.

Data availability

Data will be made available on request.

Conflicts of interest

The authors declare that they have no competing interests.

Acknowledgements

We gratefully acknowledge financial assistance from the Higher Education Commission of Pakistan, HEC-NRPU project no.20-17612/NRPU/R&D/HEC/2021 and Ongoing Research Funding program, (ORF-2025-555), King Saud University, Riyadh, Saudi Arabia.

References

1 L. G. Beka, X. Bu, X. Li, X. Wang, C. Han and W. Liu, A 2D metal–organic framework/reduced graphene oxide heterostructure for supercapacitor application, *RSC Adv.*, 2019, **9**(62), 36123–36135, DOI: 10.1039/C9RA07061C.

2 Y. Ma, X. Xie, W. Yang, Z. Yu, X. Sun, Y. Zhang, X. Yang, H. Kimura, C. Hou, Z. Guo and W. Du, Recent advances in transition metal oxides with different dimensions as electrodes for high-performance supercapacitors, *Adv. Compos. Hybrid Mater.*, 2021, **4**(4), 906–924, DOI: 10.1007/s42114-021-00358-2.

3 P. Simon, Y. Gogotsi and B. Dunn, Where Do Batteries End and Supercapacitors Begin?, *Science*, 2014, **343**(6176), 1210–1211, DOI: 10.1126/science.1249625.

4 S. Sagadevan, A. R. Marlinda, Z. Z. Chowdhury, Y. B. A. Wahab, N. A. Hamizi, M. M. Shahid, F. Mohammad, J. Podder and M. R. Johan, Fundamental electrochemical energy storage systems, *Advances in Supercapacitor and Supercapattery*, Elsevier, 2021, vol. 43, DOI: 10.1016/B978-0-12-819897-1.00001-X.

5 M. W. Mushtaq, M. Shahbaz, R. Naeem, S. Bashir, S. Sharif, K. Ali and N. A. Dogar, Synthesis of surfactant-assisted nickel ferrite nanoparticles (NFNPs@surfactant) to amplify their application as an advanced electrode material for high-

performance supercapacitors, *RSC Adv.*, 2024, **14**(28), 20230–20239, DOI: **10.1039/D4RA02135E**.

6 W. J. Basirun, I. M. Saeed, M. S. Rahman and S. A. Mazari, Nickel oxides/hydroxides-graphene as hybrid supercapattery nanocomposites for advanced charge storage materials – a review, *Crit. Rev. Solid State Mater. Sci.*, 2021, **46**(6), 553–586, DOI: **10.1080/10408436.2021.1886040**.

7 N. Zahra, M. Shahbaz, M. Saleem, M. Z. Khan, M. Irshad, S. Sharif, J. H. Koh, M. A. Marwat, G. Lee, M. Irfan and A. Ghaffar, Innovative multiphase composites of transition metal oxides for long-term stability and high energy density in storage devices, *Mater. Today Sustain.*, 2025, **30**, 101099, DOI: **10.1016/j.mtsust.2025.101099**.

8 C. Chuang and C. Kung, Metal−Organic Frameworks toward Electrochemical Sensors: Challenges and Opportunities, *Electroanalysis*, 2020, **32**(9), 1885–1895, DOI: **10.1002/elan.202060111**.

9 M. Shahbaz, M. Saeed, S. Sharif, T. T. R. Afzal, A. Ashraf, B. Riaz, Z. Ghaznavi, S. Shahzad, M. W. Mushtaq and A. Shahzad, A Review on Architecting Rationally Designed Metal-Organic Frameworks for the Next-Generation Li-S Batteries, *Small*, 2025, **21**(10), 2406613, DOI: **10.1002/smll.202406613**.

10 D. Li, A. Yadav, H. Zhou, K. Roy, P. Thanasekaran and C. Lee, Advances and Applications of Metal-Organic Frameworks (MOFs) in Emerging Technologies: A Comprehensive Review, *Glob Chall.*, 2024, **8**(2), 2300244, DOI: **10.1002/gch2.202300244**.

11 L. Zhang, Y. Wang, C. Yang and K. Tao, Metal-Organic Framework-Based Electrodes for Asymmetric Supercapacitors, *Batteries Supercaps*, 2025, **8**(4), 202400534, DOI: **10.1002/batt.202400534**.

12 Y. Luo, K. Bernot, G. Calvez, S. Freslon, C. Daiguebonne, O. Guillou, N. Kerbellec and T. Roisnel, 1,2,4,5-Benzene-tetra-carboxylic acid: a versatile ligand for high dimensional lanthanide-based coordination polymers, *CrystEngComm*, 2013, **15**(10), 1882, DOI: **10.1039/c2ce26940f**.

13 Z. Ye, Y. Jiang, L. Li, F. Wu and R. Chen, Rational Design of MOF-Based Materials for Next-Generation Rechargeable Batteries, *Nano-Micro Lett.*, 2021, **13**(1), 203, DOI: **10.1007/s40820-021-00726-z**.

14 L.-R. Yang, S. Song, C. Shao, W. Zhang, H.-M. Zhang, Z.-W. Bu and T. Ren, Synthesis, structure and luminescent properties of two-dimensional lanthanum(III) porous coordination polymer based on pyridine-2,6-dicarboxylic acid, *Synth. Met.*, 2011, **161**(11–12), 925–930, DOI: **10.1016/j.synthmet.2011.02.020**.

15 H.-L. Gao, L. Yi, B. Zhao, X.-Q. Zhao, P. Cheng, D.-Z. Liao and S.-P. Yan, Synthesis and Characterization of Metal−Organic Frameworks Based on 4-Hydroxypyridine-2,6-dicarboxylic Acid and Pyridine-2,6-dicarboxylic Acid Ligands, *Inorg. Chem.*, 2006, **45**(15), 5980–5988, DOI: **10.1021/ic060550j**.

16 M. Lammert, C. Glißmann and N. Stock, Tuning the stability of bimetallic Ce(iv)/Zr(iv)-based MOFs with UiO-66 and MOF-808 structures, *Dalton Trans.*, 2017, **46**(8), 2425–2429, DOI: **10.1039/C7DT00259A**.

17 M. Shahbaz, S. Sharif, T. T. Rehman Afzal, S. Shahzad, A. Shahzad, O. Şahin, A. Bentalib, A. Bin Jumah, S. Hussain and N. Ali Khan, Construction of rectangular microporous Cerium 3D metal organic framework for high performance energy storage devices, *J. Solid State Chem.*, 2025, **348**, 125394, DOI: **10.1016/j.jssc.2025.125394**.

18 J. Jacobsen, A. Ienco, R. D'Amato, F. Costantino and N. Stock, The chemistry of Ce-based metal–organic frameworks, *Dalton Trans.*, 2020, **49**(46), 16551–16586, DOI: **10.1039/D0DT02813D**.

19 J. H. Shah, S. Sharif, M. Shahbaz, M. Saeed, A. Shahzad, S. Farid, S. Shahzad and S. Muhammad, Electrochemical investigation of copper 1D conductive polymer for hybrid supercapacitor applications, *J. Energy Storage*, 2024, **102**, 114058, DOI: **10.1016/j.est.2024.114058**.

20 T. W. Murinzi, E. Hosten and G. M. Watkins, Synthesis and characterization of a cobalt-2,6-pyridinedicarboxylate MOF with potential application in electrochemical sensing, *Polyhedron*, 2017, **137**, 188–196, DOI: **10.1016/j.poly.2017.08.030**.

21 J. H. Shah, M. Shahbaz, S. Sharif, G. Ullah, S. Shahzad, K. S. Munawar, O. Şahin, K. Yusuf and H. Ahmad, Redox active cobalt based bi-linker metal organic frameworks derived from 5-sulfoisopthalic acid and 4,4-bipyridine for supercapacitor, *Mater. Res. Bull.*, 2025, **181**, 113123, DOI: **10.1016/j.materresbull.2024.113123**.

22 Z. Zhang, J. Dai, L. Han and K. Tao, MOF-on-MOF-derived double-shelled iron-doped cobalt sulfide nanosheet arrays modified by CeO2 for asymmetric supercapacitors, *J. Energy Storage*, 2024, **101**, 113956, DOI: **10.1016/j.est.2024.113956**.

23 M. Shahbaz, S. Sharif, M. W. Mushtaq, Z. Ghaznazvi, Z. Iqbal, M. A. Khurshid, O. Şahin, S. Shahzad, M. Saeed and A. Shahzad, Improved electrochemical performance of nitrogen-containing copper-based 1D metal organic framework derived from highly connective pyridine-2,4,6-tricarboxylic acid for hybrid supercapacitors, *J. Mater. Chem. A*, 2025, **13**(9), 6524–6538, DOI: **10.1039/D4TA05425C**.

24 P. Li, Z. Jin, L. Peng, F. Zhao, D. Xiao, Y. Jin and G. Yu, Stretchable All-Gel-State Fiber-Shaped Supercapacitors Enabled by Macromolecularly Interconnected 3D Graphene/Nanostructured Conductive Polymer Hydrogels, *Adv. Mater.*, 2018, **30**(18), 1800124, DOI: **10.1002/adma.201800124**.

25 Z. Jin, P. Li, Y. Jin and D. Xiao, Superficial-defect engineered nickel/iron oxide nanocrystals enable high-efficient flexible fiber battery, *Energy Storage Mater.*, 2018, **13**, 160–167, DOI: **10.1016/j.ensm.2018.01.010**.

26 U. A. Khan, N. Iqbal, T. Noor, R. Ahmad, A. Ahmad, J. Gao, Z. Amjad and A. Wahab, Cerium based metal organic framework derived composite with reduced graphene oxide as efficient supercapacitor electrode, *J. Energy Storage*, 2021, **41**, 102999, DOI: **10.1016/j.est.2021.102999**.

27 X.-J. Hong, C.-L. Song, Y. Yang, H.-C. Tan, G.-H. Li, Y.-P. Cai and H. Wang, Cerium Based Metal–Organic Frameworks as an Efficient Separator Coating Catalyzing the Conversion of Polysulfides for High Performance Lithium–Sulfur

Batteries, *ACS Nano*, 2019, **12**(2), 1923–1931, DOI: 10.1021/acsnano.8b08155.

28 P. Wen, Z. Li, P. Gong, J. Sun, J. Wang and S. Yang, Design and fabrication of carbonized rGO/CMOF-5 hybrids for supercapacitor applications, *RSC Adv.*, 2016, **6**(16), 13264–13271, DOI: 10.1039/C5RA27893G.

29 X. Cao, B. Zheng, W. Shi, J. Yang, Z. Fan, Z. Luo, X. Rui, B. Chen, Q. Yan and H. Zhang, Reduced Graphene Oxide-Wrapped MoO 3 Composites Prepared by Using Metal–Organic Frameworks as Precursor for All-Solid-State Flexible Supercapacitors, *Adv. Mater.*, 2015, **27**(32), 4695–4701, DOI: 10.1002/adma.201501310.

30 P. C. Banerjee, D. E. Lobo, R. Middag, W. K. Ng, M. E. Shaibani and M. Majumder, Electrochemical Capacitance of Ni-Doped Metal Organic Framework and Reduced Graphene Oxide Composites: More than the Sum of Its Parts, *ACS Appl. Mater. Interfaces*, 2015, **7**(6), 3655–3664, DOI: 10.1021/am508119c.

31 Y. Zhong, X. Cao, L. Ying, L. Cui, C. Barrow, W. Yang and J. Liu, Homogeneous nickel metal-organic framework microspheres on reduced graphene oxide as novel electrode material for supercapacitors with outstanding performance, *J. Colloid Interface Sci.*, 2020, **561**, 265–274, DOI: 10.1016/j.jcis.2019.10.023.

32 E. L. Subtil, J. Gonçalves, H. G. Lemos, E. C. Venancio, J. C. Mierzwa, J. dos Santos de Souza, W. Alves and P. Le-Clech, Preparation and characterization of a new composite conductive polyethersulfone membrane using polyaniline (PANI) and reduced graphene oxide (rGO), *Chem. Eng. J.*, 2020, **390**, 124612, DOI: 10.1016/j.cej.2020.124612.

33 X. Cai, K. Sun, Y. Qiu and X. Jiao, Recent Advances in Graphene and Conductive Polymer Composites for Supercapacitor Electrodes: A Review, *Crystals*, 2021, **11**(8), 947, DOI: 10.3390/cryst11080947.

34 S. H. Kang, G. Y. Lee, J. Lim and S. O. Kim, CNT–rGO Hydrogel-Integrated Fabric Composite Synthesized via an Interfacial Gelation Process for Wearable Supercapacitor Electrodes, *ACS Omega*, 2021, **6**(30), 19578–19585, DOI: 10.1021/acsomega.1c02091.

35 D. K. Singha, R. I. Mohanty, P. Bhanja and B. K. Jena, Metal–organic framework and graphene composites: advanced materials for electrochemical supercapacitor applications, *Mater. Adv.*, 2023, **4**(20), 4679–4706, DOI: 10.1039/D3MA00523B.

36 M. A. Nazir, M. S. Javed, M. Islam, M. A. Assiri, A. M. Hassan, M. Jamshaid, T. Najam, S. S. A. Shah and A. ur. Rehman, MOF@graphene nanocomposites for energy and environment applications, *Compos. Commun.*, 2024, **45**, 101783, DOI: 10.1016/j.coco.2023.101783.

37 Q. V. Thi, S. A. Patil, P. K. Katkar, I. Rabani, A. S. Patil, J. Ryu, G. Kolekar, N. T. Tung and D. Sohn, Electrochemical performance of zinc-based metal-organic framework with reduced graphene oxide nanocomposite electrodes for supercapacitors, *Synth. Met.*, 2022, **290**, 117155, DOI: 10.1016/j.synthmet.2022.117155.

38 M. Shahbaz, S. Sharif, A. Shahzad, Z. S. Şahin, B. Riaz and S. Shahzad, Enhanced electrochemical performance of cerium-based metal organic frameworks derived from pyridine-2,4,6-tricarboxylic acid for energy storage devices, *J. Energy Storage*, 2024, **88**, 111463, DOI: 10.1016/j.est.2024.111463.

39 D. Mohanadas, M. A. A. Mohd Abdah, N. H. N. Azman, J. Abdullah and Y. Sulaiman, A promising negative electrode of asymmetric supercapacitor fabricated by incorporating copper-based metal-organic framework and reduced graphene oxide, *Int. J. Hydrogen Energy*, 2021, **46**(71), 35385–35396, DOI: 10.1016/j.ijhydene.2021.08.081.

40 M. Sathiya, A. S. Prakash, K. Ramesha, J. Tarascon and A. K. Shukla, V 2 O 5 -Anchored Carbon Nanotubes for Enhanced Electrochemical Energy Storage, *J. Am. Chem. Soc.*, 2011, **133**(40), 16291–16299, DOI: 10.1021/ja207285b.

41 S.-B. Xia, S.-W. Yu, L.-F. Yao, F.-S. Li, X. Li, F.-X. Cheng, X. Shen, C.-K. Sun, H. Guo and J.-J. Liu, Robust hexagonal nut-shaped titanium(IV) MOF with porous structure for ultra-high performance lithium storage, *Electrochim. Acta*, 2019, **296**, 746–754, DOI: 10.1016/j.electacta.2018.11.135.

42 S. Sundriyal, V. Shrivastav, H. Kaur, S. Mishra and A. Deep, High-Performance Symmetrical Supercapacitor with a Combination of a ZIF-67/rGO Composite Electrode and a Redox Additive Electrolyte, *ACS Omega*, 2018, **3**(12), 17348–17358, DOI: 10.1021/acsomega.8b02065.

43 Nonius, *COLLECT*, Nonius BV, Delft, The Netherlands, 2001.

44 Z. Otwinowski, W. Minor, [20] Processing of X-ray diffraction data collected in oscillation mode, 1997, pp. 307–326, DOI: 10.1016/S0076-6879(97)76066-X.

45 C. F. Macrae, I. J. Bruno, J. A. Chisholm, P. R. Edgington, P. McCabe, E. Pidcock, L. Rodriguez-Monge, R. Taylor, J. van de Streek and P. A. Wood, Mercury CSD 2.0 – new features for the visualization and investigation of crystal structures, *J. Appl. Crystallogr.*, 2008, **41**(2), 466–470, DOI: 10.1107/S0021889807067908.

46 L. J. Farrugia, *J. Appl. Crystallogr.*, 1999, **32**, 837–838.

47 J. Heinze, Cyclic Voltammetry—"Electrochemical Spectroscopy". New Analytical Methods (25), *Angew. Chem., Int. Ed. Engl.*, 1984, **23**(11), 831–847, DOI: 10.1002/anie.198408313.

48 F. Scholz, A. M. Bond, R. G. Compton, D. A. Fiedler, G. Inzelt, H. Kahlert, Š. Komorsky-Lovrić, H. Lohse, M. Lovrić, F. Marken, A. Neudeck, U. Retter, F. Scholz, Z. Stojek, *Electroanalytical Methods*, Springer Berlin Heidelberg, Berlin, Heidelberg, 2010, DOI: 10.1007/978-3-642-02915-8.

49 K. J. Aoki, J. Chen, Y. Liu and B. Jia, Peak potential shift of fast cyclic voltammograms owing to capacitance of redox reactions, *J. Electroanal. Chem.*, 2020, **856**, 113609, DOI: 10.1016/j.jelechem.2019.113609.

50 K. Kowsuki, R. Nirmala, Y.-H. Ra and R. Navamathavan, Recent advances in cerium oxide-based nanocomposites in synthesis, characterization, and energy storage applications: A comprehensive review, *Results Chem.*, 2023, **5**, 100877, DOI: 10.1016/j.rechem.2023.100877.

51 T. Liu, G. Lv, M. Liu, X. Cui, H. Liu, H. Li, C. Zhao, L. Wang, J. Guo and L. Liao, MOF-Derived Nitrogen-Rich Hollow

Nanocages as a Sulfur Carrier for High-Voltage Aluminum Sulfur Batteries, *ACS Nano*, 2024, **18**(45), 31559–31568, DOI: **10.1021/acsnano.4c13092**.

52 M. K. Singh, A. K. Gupta, S. Krishnan, N. Guha, S. Marimuthu and D. K. Rai, A new hierarchically porous Cu-MOF composited with rGO as an efficient hybrid supercapacitor electrode material, *J. Energy Storage*, 2021, **43**, 103301, DOI: **10.1016/j.est.2021.103301**.

53 Q. Gong, Y. Li, H. Huang, J. Zhang, T. Gao and G. Zhou, Shape-controlled synthesis of Ni-CeO2@PANI nanocomposites and their synergetic effects on supercapacitors, *Chem. Eng. J.*, 2018, **344**, 290–298, DOI: **10.1016/j.cej.2018.03.079**.

54 X. Li, J. Li, Y. Zhang and P. Zhao, Synthesis of Ni-MOF derived NiO/rGO composites as novel electrode materials for high performance supercapacitors, *Colloids Surf., A*, 2021, **622**, 126653, DOI: **10.1016/j.colsurfa.2021.126653**.

55 Z. Karimzadeh, B. Shokri and A. Morsali, Rapid cold plasma synthesis of cobalt metal–organic framework/reduced graphene oxide nanocomposites for use as supercapacitor electrodes, *Sci. Rep.*, 2023, **13**(1), 15156, DOI: **10.1038/s41598-023-41816-9**.

56 A. Gowdhaman, S. A. Kumar, D. Elumalai, C. Balaji, M. Sabarinathan, R. Ramesh and M. Navaneethan, Ni-MOF derived NiO/Ni/r-GO nanocomposite as a novel electrode material for high-performance asymmetric supercapacitor, *J. Energy Storage*, 2023, **61**, 106769, DOI: **10.1016/j.est.2023.106769**.

57 M. Majumder, R. B. Choudhary, A. K. Thakur, A. Khodayari, M. Amiri, R. Boukherroub and S. Szunerits, Aluminum based metal-organic framework integrated with reduced graphene oxide for improved supercapacitive performance, *Electrochim. Acta*, 2020, **353**, 136609, DOI: **10.1016/j.electacta.2020.136609**.

58 C. Ren, X. Jia, W. Zhang, D. Hou, Z. Xia, D. Huang, J. Hu, S. Chen and S. Gao, Hierarchical Porous Integrated Co 1−x S/CoFe 2 O 4 @rGO Nanoflowers Fabricated via Temperature-Controlled In Situ Calcining Sulfurization of Multivariate CoFe-MOF-74@rGO for High-Performance Supercapacitor, *Adv. Funct. Mater.*, 2020, **30**(45), 2004519, DOI: **10.1002/adfm.202004519**.

59 M. Fallah barzoki, S. Fatemi and M. R. Ganjali, Fabrication and comparison of composites of cerium metal-organic framework/reduced graphene oxide as the electrode in supercapacitor application, *J. Energy Storage*, 2022, **55**, 105545, DOI: **10.1016/j.est.2022.105545**.